

MDPI

Article

Electrochemical Activity of Original and Infiltrated Fe-Doped Ba(Ce,Zr,Y)O₃-Based Electrodes to Be Used for Protonic Ceramic Fuel Cells

Liana R. Tarutina ^{1,2,*}, Anna V. Kasyanova ^{1,2}, George N. Starostin ², Gennady K. Vdovin ¹ and Dmitry A. Medvedev ^{1,2,*}

- Laboratory of Electrochemical Devices Based on Solid Oxide Proton Electrolytes, Institute of High Temperature Electrochemistry, 620990 Ekaterinburg, Russia
- ² Hydrogen Energy Laboratory, Chemical Engineering Institute, Ural Federal University, 620002 Ekaterinburg, Russia
- * Correspondence: hakimovaliana@rambler.ru (L.R.T.); dmitrymedv@mail.ru (D.A.M.)

Abstract: Proton-ceramic fuel cells (PCFCs) are promising devices for electrochemical energy conversion purposes due to their combination of high energy efficiency, environmental friendliness, and high durability. In the present work, the polarization characteristics of promising electrodes for PCFCs based on BaFe_xCe_{0.7-x}Zr_{0.2}Y_{0.1}O_{3-\delta} (BCZYFx) are comprehensively studied. Along with the individual BCZYFx electrodes, we investigated a method for improving their electrochemical activity by introducing nanoparticles of PrO_x electrocatalysts into the porous structure of the electrode material. According to the experimental data, electroactivation allowed for the polarization resistances of the electrodes at 700 °C to be reduced from 1.16, 0.27, 0.62 Ω° cm² to 0.09, 0.13, 0.43 Ω° cm² for x = 0.5, 0.6, and 0.7, respectively. For a PCFC cell with an air electrode of BCZYF0.6 composition activated using PrO_x nanoparticles, it was possible to achieve a maximum specific power of 300 mW cm⁻² at 750 °C, which is competitive for a single cell with Co-free cathodes. The results obtained provide insight into the processes occurring in the studied electrodes after electroactivation. It is shown how the improvement of electrochemical characteristics of the electrode can be realized by a simple infiltration method in combination with a subsequent thermal treatment.

Keywords: PCFCs; electrode materials; proton conduction; infiltration; electrochemical activity



Citation: Tarutina, L.R.; Kasyanova, A.V.; Starostin, G.N.; Vdovin, G.K.; Medvedev, D.A. Electrochemical Activity of Original and Infiltrated Fe-Doped Ba(Ce,Zr,Y)O₃-Based Electrodes to Be Used for Protonic Ceramic Fuel Cells. *Catalysts* **2022**, *12*, 1421. https://doi.org/10.3390/catal12111421

Academic Editors: Farid Orudzhev and Irina A. Zvereva

Received: 19 October 2022 Accepted: 9 November 2022 Published: 12 November 2022

Publisher's Note: MDPI stays neutral with regard to jurisdictional claims in published maps and institutional affiliations.



Copyright: © 2022 by the authors. Licensee MDPI, Basel, Switzerland. This article is an open access article distributed under the terms and conditions of the Creative Commons Attribution (CC BY) license (https://creativecommons.org/licenses/by/4.0/).

1. Introduction

The problem of creating environmentally safe and highly efficient energy conversion devices is increasingly attracting the attention of the scientific community due to increasing levels of global energy consumption and depletion of mineral resources [1,2]. As a possible solution to these problems, solid oxide fuel cells (SOFC) based on oxygen or protonconducting electrolytes have been proposed. Among the important advantages of SOFCs are their ability to convert a wide range of fuels varying in their purity, their high energy efficiency, and the absence of harmful emissions [3–5]. While most of the research has been focused on oxygen-ion electrolyte-based SOFCs, the high operating temperatures involved, which are associated with degradation processes, restrict their commercialization [6–9]. The use of proton-ceramic fuel cells (PCFCs) is considered as an efficient means, which reduce the operating temperature to 500-800 °C without a significant increase in the total resistance of electrochemical cells [10-14]. One of the most promising representatives of protonconducting electrolytes for PCFCs are phases based on barium cerate-zirconates [15,16]. Among the complex oxide electrolyte materials, these electrolytes demonstrate the highest values of ionic (including protonic) conductivity, good hydration capability, and low electron transfer numbers [15,17–19].

A concomitant important step in the design of PCFCs is the need to develop efficient and stable air electrodes offering high electrochemical activity at moderate temperatures

Catalysts **2022**, 12, 1421 2 of 16

for the successful facilitation of oxygen reduction reaction (ORR) [20–22]. Cobalt-based perovskites are the most investigated cathode materials due to their mixed ion-electron conductivity characterized by high electrochemical activity toward ORR [23,24]. However, the thermomechanical incompatibility between these electrodes and proton-conducting electrolytes raises serious issues concerning their application under real conditions, when PCFCs are tested in thermo- and redox-cycling modes [25–27].

Co-free complex oxides based on BaFeO₃ offer a promising alternative to the already known cathode materials due to their satisfactory electrical conductivity [28,29]. In contrast to cathodes containing expensive cobalt, these modified ferrites also have acceptable thermal expansion coefficients; this allows for the avoidance of thermomechanical mismatch with proton-conducting electrolytes during real PCFC operation conditions [30,31]. Moreover, recent studies [32–36] confirm prospects of BaFeO₃-based electrodes from the transport viewpoint. In detail, doped BaFeO₃ enables fact conduction of both oxygen- and proton-charge carries, improving considerably ORR kinetics in PCFCs compared to solely conductive systems. However, the electrochemical characteristics of existing barium ferrite materials require additional optimization. One of the suitable methods to solve this problem is to modify the electrode structure by infiltration with nanoparticles of electrochemically active oxide particles [14,37–39].

In the present work, complex oxides of the BaFe $_x$ Ce $_{0.7-x}$ Zr $_{0.2}$ Y $_{0.1}$ O $_{3-\delta}$ compositions are considered as oxygen (air) electrodes of PCFCs. The basic barium ferrite was doped with cerium and yttrium to improve the transport properties, while zirconium doping was used to improve the chemical stability of the cathode materials. The aim of the work was to investigate and modify the electrochemical characteristics of PCFC electrode materials of BaFe $_x$ Ce $_{0.7-x}$ Zr $_{0.2}$ Y $_{0.1}$ O $_{3-\delta}$ by introducing PrO $_x$ nanoparticles into their porous structure.

2. Results and Discussion

2.1. Quality of the Prepared Materials

According to the X-ray phase analysis results, both the obtained electrodes and the electrolyte form single-phase perovskite structures without any impurity phases. The studied BCZYFx cathodes are characterized by a cubic structure with the space group of $Pm\overline{3}m$ (Figure 1a) [40]. The increase in the iron concentration leads to a shift of the XRD pattern reflections toward larger angles, providing evidence of a decrease in the unit cell volume (Figure 1b). This result is expected due to the lower ionic radii of iron-ions (0.56 Å) as compared to Ce⁴⁺-ions (0.87 Å) [41]. The BCZYYb electrolyte forms a perovskite tetragonal structure with the space group of $R\overline{3}c$ (Figure 1c) [42].

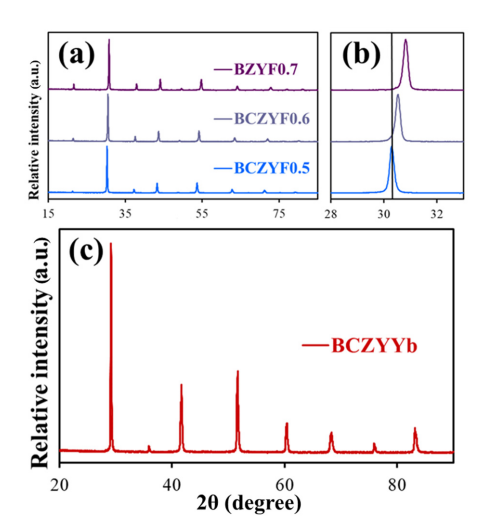


Figure 1. XRD patterns of the ceramic cathode samples after sintering at 1350 °C (**a**), XRD patterns in a narrow angle range (**b**), XRD results for the ceramic electrolyte sample following its sintering at 1450 °C (**c**).

Catalysts 2022, 12, 1421 3 of 16

2.2. Performance of the BaFe_xCe_{0.7-x}Zr_{0.2}Y_{0.1}O_{3- δ}-Based Electrodes on Symmetrically Designed Cells

2.2.1. Microstructural Analysis

Microstructural features of the cross-section for the SDCs are presented in Figure 2. Due to the measurements being carried out under an unseparated gas environment, the electrolyte characteristics (thickness, density) were not taken into account. The porosity of cathode layers measured using the ImageJ software was 35–40%, while the electrode thickness was about 10 μm [43]. The results of EDX spectroscopy presented in Figure 3 demonstrate good adhesion of the electrode to the electrolyte and the absence of diffusion traces between the SDC functional layers.

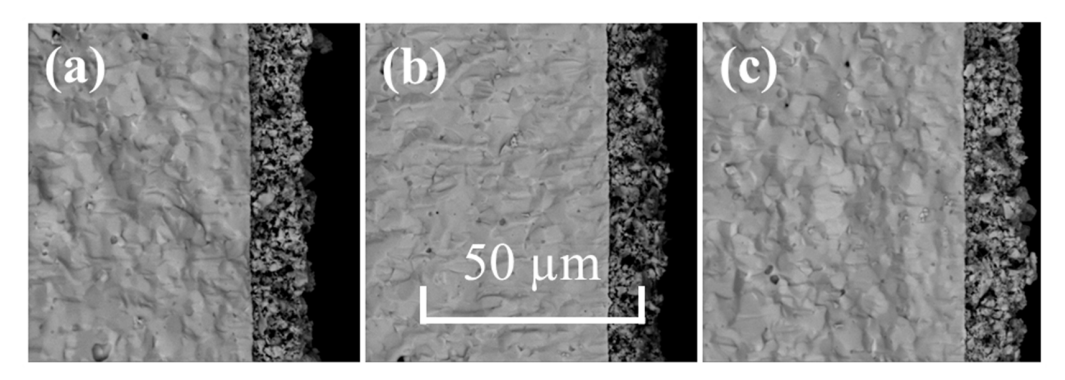


Figure 2. Microphotographs of symmetric configuration cells after electrode sintering of compositions: BCZYF0.5 (a), BCZYF0.6 (b), BZYF0.7 (c).

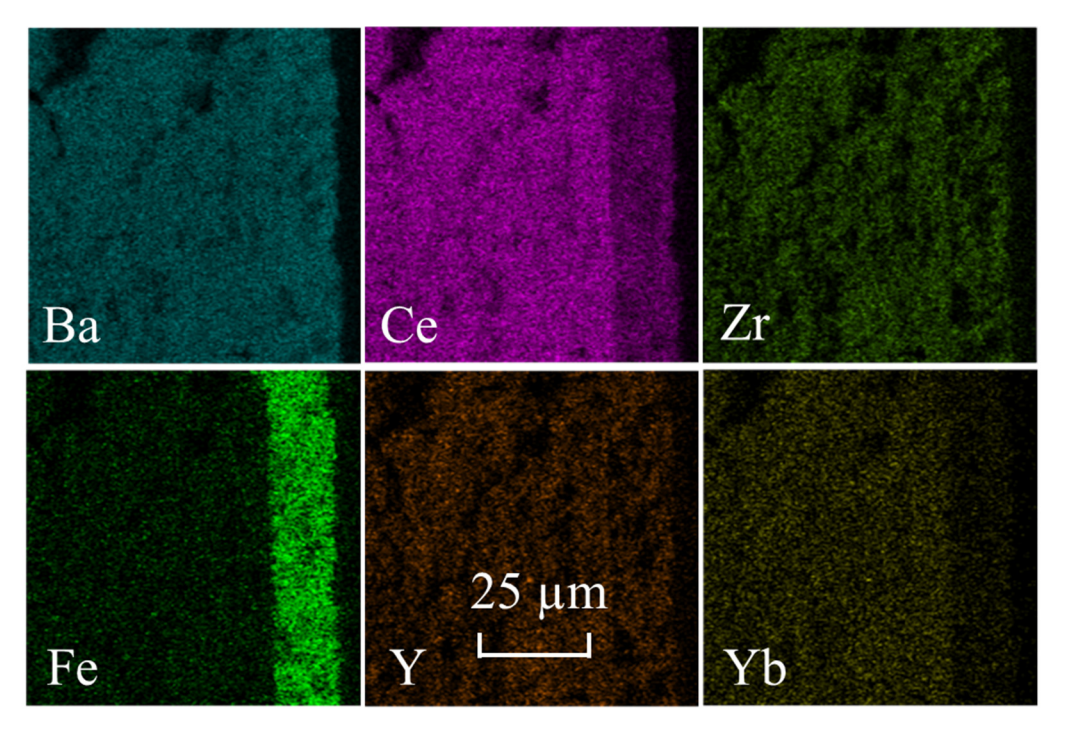


Figure 3. Distribution maps of main elements in the SDC with the BCZYF0.5 non-activated electrode.

The distribution of electrochemically active PrO_x nanoparticles following the annealing of the sample at 600 °C was assessed using the EDX method. As shown in Figure 4, the infiltration method preserved good permeability of the electroactivator into the porous electrode volume without sealing of the electrode after heat treatment. In addition, the absence of a praseodymium oxide layer on the surface of the BCZYFx material prevents degradation of polarization characteristics due to reduced gas diffusion.

Catalysts **2022**, 12, 1421 4 of 16

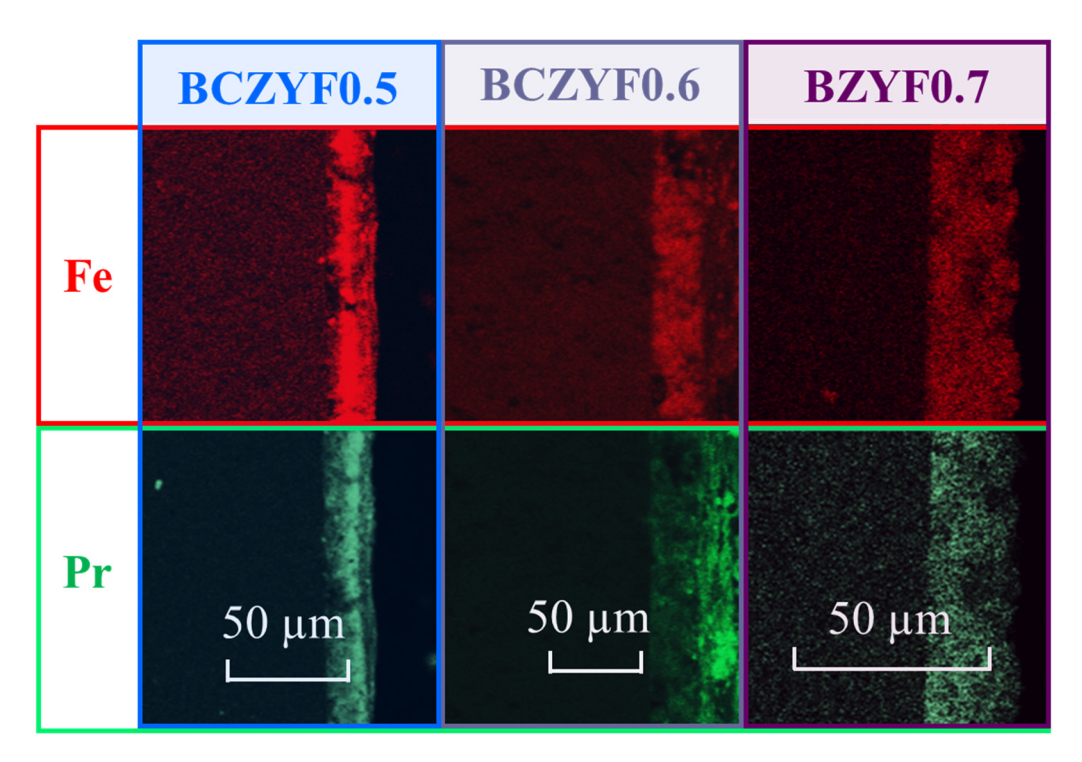


Figure 4. Distribution maps of iron and infiltrated praseodymium in the porous cathodes after isothermal treatment at 600 °C.

2.2.2. Polarization Characteristics

To estimate the effect of PrO_x infiltration on the electrochemical characteristics of the air electrodes, the EIS of SDC was carried out in air at 600–800 °C. Figure 5a shows the impedance hodographs in Nyquist coordinates for BCZYF0.6 samples before and after electroactivation. To compare the polarization resistances of the electrodes, the ohmic resistance was subtracted from the total impedance. Furthermore, the total polarization resistance values of the studied cathodes were calculated by the equivalent circuits method (Figure 5b). Although infiltration has a favorable effect on the polarization resistance level, leading to its reduction in the entire range of iron concentrations, the best effect is observed at low iron concentrations in the electrodes. Therefore, the observed decrease in polarization resistance at 750 °C is approximately 93, 50, and 27% for x = 0.5, 0.6, and 0.7, respectively.

Previously, we published an investigation covering the conductivity of electrodes based on barium cerate-zirconates doped with iron in a wide range of its concentration [44]. With the increasing iron content from x = 0.5 to x = 0.7 at 900 °C and at a partial pressure of oxygen (pO_2) equal to 10^{-10} atm, the ionic component of conductivity increased from approximately 7 to 55 mS cm⁻¹. However, the increase in electronic conductivity was more significant at the same temperature (from 150 to 860 mS cm⁻¹ at pO₂ = 0.21 atm) due to the presence of the Fe^{4+}/Fe^{3+} redox-pair and the increased concentration of iron ions in the perovskite structure. Namely, BCZYF0.5, BCZYF0.6, and BCZYF0.7 are mixed ionic-electronic conductors, in which both ionic and electronic conductivities increase with the growing iron concentration. The revealed effects of infiltration can be explained by connecting the results obtained for individual ceramic materials with the data of the current study. Therefore, while the BCZYF0.5 electrode does not offer the best transport characteristics, infiltration improves the rate-determining stages and significantly reduces the polarization resistance of the electrode. Since the BCZYF0.7 electrode material has its own high mixed ionic-electronic conductivity, infiltration does not significantly reduce the polarization characteristics of this electrode. Figure A1 shows the impedance spectra of samples with x = 0.5-0.7 at 600 °C. Substantial differences in spectra for the sample with x = 0.5 before and after activation may indicate an improvement in overall electrode processes. A further increase in the iron concentration leads to a gradual leveling of the effect of the introduction of PrO_x nanoparticles. Based on

Catalysts **2022**, 12, 1421 5 of 16

the foregoing, we can conclude that the lower the initial level of ion-electron conductivity of the material of the electrodes under study, the more pronounced and positive effect the infiltration has on their polarization characteristics.

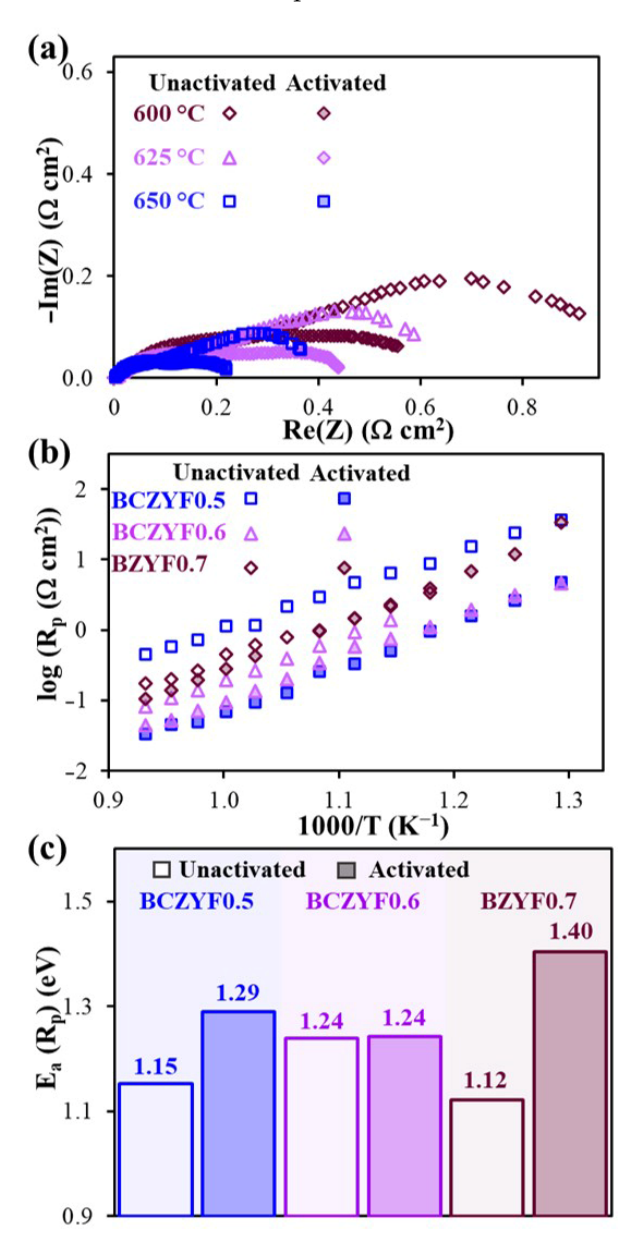


Figure 5. Electrochemical results obtained for the SDCs with the origin (unactivated) and electroactivated BCZYFx electrodes: (a) impedance spectra for BCZYF0.6 at various temperatures, (b) temperature dependences of polarization resistances, and (c) the apparent activation energies.

To evaluate the electrochemical characteristics of BaFe $_x$ Ce $_{0.7-x}$ Zr $_{0.2}$ Y $_{0.1}$ O $_{3-\delta}$, the obtained values of polarization resistances were compared with the data obtained for various electrodes based on barium ferrites. According to Table 1, the electrodes at 600 °C before and after electroactivation are characterized by rather high polarization resistances inferior to values of other electrodes, which complicates their operation. Nevertheless, at 700 °C, the material with x = 0.6 has competitive characteristics both in the initial state, and following infiltration by praseodymium nitrate. This makes the electrode material of BaFe $_{0.6}$ Ce $_{0.1}$ Zr $_{0.2}$ Y $_{0.1}$ O $_{3-\delta}$ composition interesting for further studies as an air electrode for PCFCs.

Catalysts 2022, 12, 1421 6 of 16

Table 1. Polarization resistances of BaFeO₃-based electrodes obtained for SDCs with an electrode | electrolyte | electrode configuration.

Electrode Materials	Electrolyte Materials	R_p (Ω° cm ²)		D. C
		600 °C	700 °C	— Ref.
$BaFe_{0.5}Ce_{0.2}Zr_{0.2}Y_{0.1}O_{3-\delta}$	$BaCe_{0.5}Zr_{0.3}Y_{0.1}Yb_{0.1}O_{3-\delta}$	6.54	1.16	This work
BaFe _{0.5} Ce _{0.2} Zr _{0.2} Y _{0.1} O _{3-δ} Pr		0.50	0.09	
BaFe _{0.6} Ce _{0.1} Zr _{0.2} Y _{0.1} O _{3-δ}		1.40	0.27	
BaFe _{0.6} Ce _{0.1} Zr _{0.2} Y _{0.1} O _{3-δ} Pr		0.75	0.13	
BaFe _{0.7} Zr _{0.2} Y _{0.1} O _{3-δ}		2.20	0.62	
$BaFe_{0.7}Zr_{0.2}Y_{0.1}O_{3-\delta}_Pr$		2.32	0.43	
$Bi_{0.5}Ba_{0.5}FeO_{3-\delta}$	$BaZr_{0.1}Ce_{0.7}Y_{0.2}O_{3-\delta}$	1.01	0.19	[45]
BaCe _{0.05} Fe _{0.95} O _{3-δ}	Sm _{0.2} Ce _{0.8} O _{1.9}	0.19	0.05	[46]
BaFe $_{0.9}$ Zr $_{0.1}$ O $_{3-\delta}$	$La_{0.9}Sr_{0.1}Ga_{0.8}Mg_{0.2}O_{3-\delta}$	0.14	0.02	[47]
$BaFe_{0.9}Nb_{0.1}O_{3-\delta}$	GDC	-	0.10	[48]
BaCe $_{0.2}$ Fe $_{0.8}$ O $_{3-\delta}$	$BaZr_{0.1}Ce_{0.7}Y_{0.2}O_{3-\delta}$	0.33	0.09	[49]
BaCe _{0.2} Fe _{0.7} Pr _{0.1} O _{3-δ}		0.25	0.07	
BaCe _{0.2} Fe _{0.6} Pr _{0.2} O _{3-δ}		0.23	0.20	
BaCe _{0.2} Fe _{0.5} Pr _{0.3} O _{3-δ}		0.51	0.14	
BaFe _{0.95} Pr _{0.05} O _{3-δ}	$Ce_{0.9}Gd_{0.1}O_{2-\delta}$	0.42	0.10	 [50]
BaFe _{0.9} Pr _{0.1} O _{3$-\delta$}		0.68	0.14	
BaFe _{0.85} Pr _{0.15} O _{3-δ}		0.82	0.17	
BaFe _{0.8} Pr _{0.2} O _{3$-\delta$}		1.68	0.32	

The sample with an average iron concentration (x = 0.6) combines an acceptable polarization resistance both before and after electroactivation. Therefore, a more in-depth analysis of the effect of infiltration on polarization was performed for this oxide system. Clearly, the infiltration leads not only to a decrease in the polarization resistance of the electrode, but also to a change in the impedance spectrum profile (Figure 5a), indicating the influence of infiltrated PrO_x nanoparticles on the rate-determined stages of the proceeding electrode reactions. Figure 6a,b shows an equivalent diagram and an example of fitting for the BCZYF0.6 electrode at 650 °C before and after electroactivation, respectively. In the equivalent schemes, L represents the inductive element connected with current leads; R_O is the ohmic resistance; the constant phase element (Q_n) represents the non-ideal capacitor; and R_n is the polarization resistance of the corresponding electrode process. Each R_n – Q_n element represents a separate stage of the electrode process (P_n).

As can be seen from Figure 5a, the high-frequency process (P_1) in both activated and non-activated samples remains without significant changes. This may be due to the fact that P_1 probably corresponds to interfacial charge transfer or charge transfer over the electrode volume. The medium-frequency P_2 process in the non-activated electrode may correspond to oxygen dissociation and surface diffusion [51,52]. In addition, in the equivalent circuit used in the fitting of this electrode, there exists a low-frequency process P_3 , probably corresponding to gas-phase diffusion and molecular oxygen diffusion. In the activated electrode, P_2 corresponds to low-frequency processes that may be characterized by oxygen adsorption, dissociation, charge transfer, and molecular diffusion [53,54]. Infiltration leads to the fact that the P_3 process is no longer observed on the impedance spectra of the activated sample. This behavior may be due to the fact that it has exceeded the sensitivity limits of the equipment due to a significant decrease in the resistance or capacitance of the process. The values of the polarization resistance of the high-frequency P_1 process of the activated and non-activated electrode are very close to each other (Figure 6c). This is

Catalysts 2022, 12, 1421 7 of 16

natural since this process is unaffected by the PrO_x nanoparticles. In turn, the activated P_2 has lower values of polarization resistance compared to non-activated.

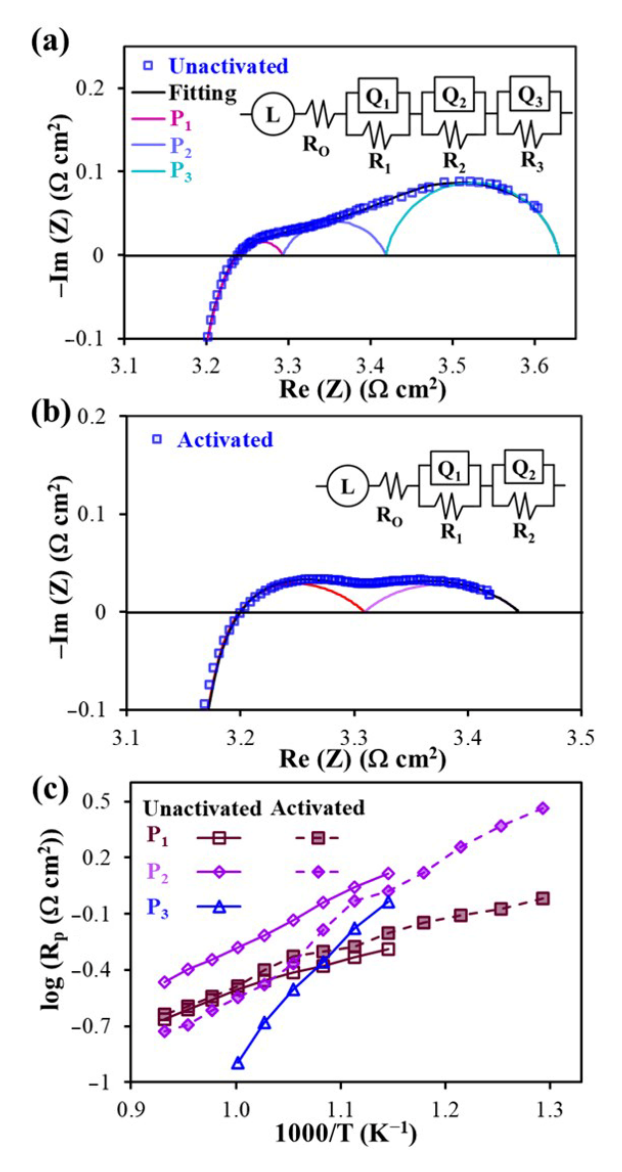


Figure 6. Equivalent diagrams and an example of fitting of BCZYF0.6 electrode before (a) and after (b) electroactivation and polarization conductivities (c), electrode processes of BCZYF0.6 (not shaded), and BCZYF0.6_Pr samples (shaded markers).

The maximum capacitance values (f_{max}) (Figure 7a) calculated for each electrode process indicate that the frequencies in the P_1 processes have close values before and after electroactivation. The observed decrease in f_{max} for P_2 following infiltration characterizes the decrease in the rate of this process. Therefore, we can conclude that the formation of electrochemically active PrO_x nanoparticles on the surface of the porous cathode favorably affects the surface exchange of BCZYF-based air electrodes. Figure 7b shows the calculated capacitances of the electrode processes. Along with the closeness of their values in the presence or absence of activation, the regular dynamics of the P_1 , P_2 , and P_3 process capacitance values indicate the common nature of these individual processes at different temperatures.

Catalysts 2022, 12, 1421 8 of 16

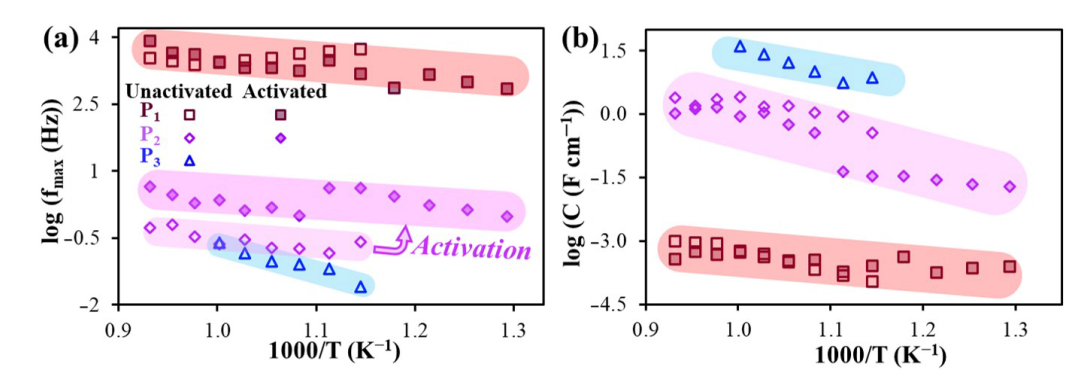


Figure 7. Frequencies (**a**) and capacitances (**b**) determined by fitting impedance spectra corresponding to electrode processes in SDC of the composition $BCZYb_{funct} \mid BCZYF0.6_{porous}$.

2.3. Characterization of a Protonic Ceramic Electrolysis Cell with BCZYF0.6-Based Cathode 2.3.1. Microstructural Analysis

Prior to the voltammetry studies, each PCFC was examined using scanning electron microscopy. Figure 8 shows four well-adhesion layers: SFEL—supporting fuel electrode layer; FFEL—functional fuel electrode layer; EL—electrolyte layer; FOEL—functional oxygen electrode layer. The thickness of each layer is about 650, 40, 25, and 10 μm , respectively. The porosity of the SFEL (NiO-BCZYYb) was determined using the ImageJ software and was about 45%. This porosity is due to the features of sintering of the oxide composite, as well as the addition of a pore-former (potato starch) in the amount of 20 wt% to the NiO and BCZYYb mixture. Figure 8b shows the cross-section of the PCFC with the infiltrated BCZYF0.6 air electrode. As in the case of symmetric cells, PrOx particles do not cause sealing or degradation of the electrode following annealing at 600 °C. The EDX results obtained for the samples after isothermal aging at 600 °C are shown in Figure 9. Praseodymium oxide is uniformly distributed over the volume of the porous air electrode; there is no concentrated activator layer on the cathode surface.

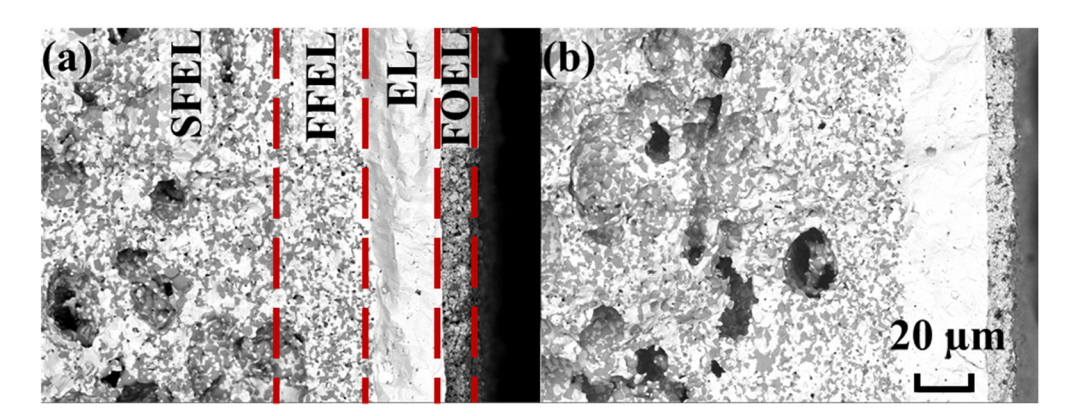


Figure 8. Cross-sectional view of the fabricated PCFC using BCZYF0.6 electrode before (a) and after (b) electroactivation.

Catalysts 2022, 12, 1421 9 of 16

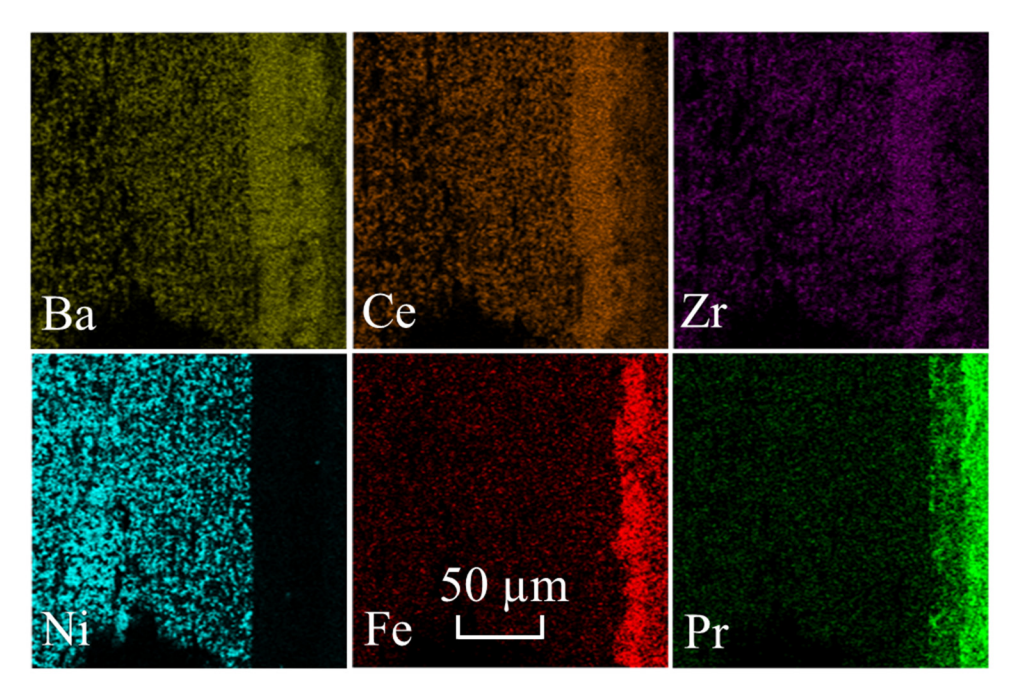


Figure 9. Element distribution maps for the PCFC with the BCZYF0.6 electrode following PrO_x electroactivation.

The single PCFC was not deformed following electrochemical measurements. The dense electrolyte remained impermeable, indicating the absence of cracks or through pores. A visual evaluation of the sample and microphotographs suggests a good adhesion between all functional materials and the absence of diffusion between them. In addition, the EDX results (Figure 10) demonstrate the absence of large agglomerates consisting of nickel (for the anodic layer) and praseodymium particles (for the cathodic layer), which can reduce the electrochemical reaction.

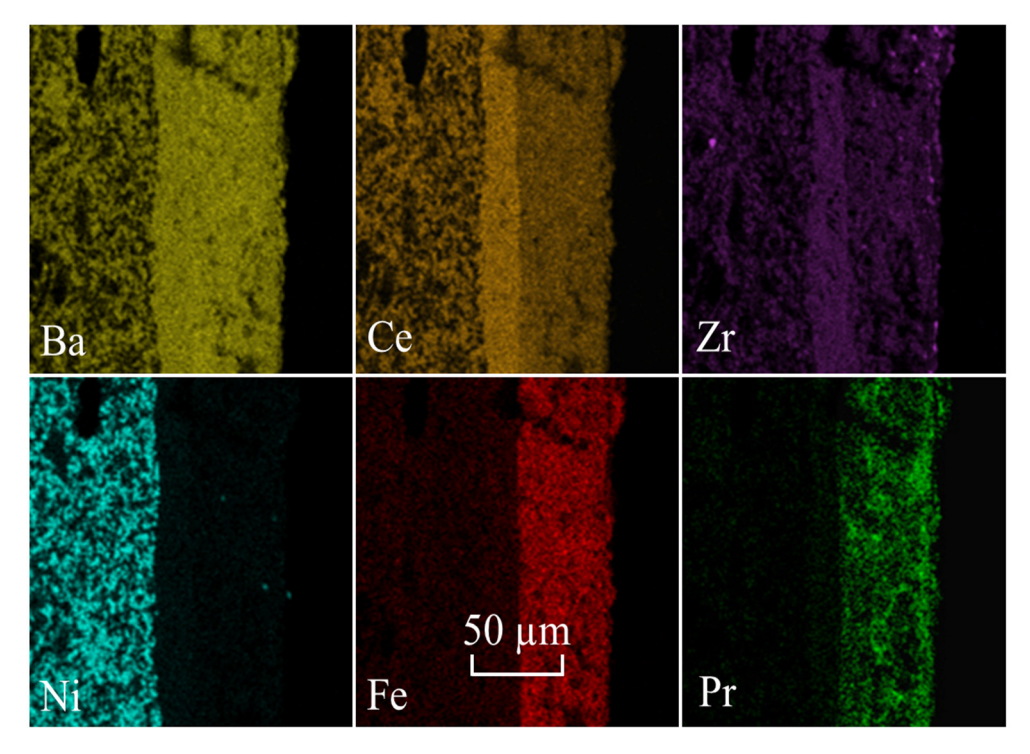


Figure 10. PCFC element distribution map with BCZYF0.6 activated electrode after electrochemical measurements.

Catalysts 2022, 12, 1421 10 of 16

2.3.2. Voltammetric Characteristics

The electrochemical characteristics of a single reversible cell with air electrode BCZYF0.6 were evaluated using the I–P curves of the NiO-BCZYYb | BCZYFb | BCZYFx single cell, as shown in Figure 11a. The fuel space was fed with humidified hydrogen and the oxygen space with humidified air. The maximum achieved specific power (P_{max}) at 700 °C was 250 mW cm⁻². These values are comparable with other PCFCs with barium ferrite cathodes. For example, for BaFe_{0.9}Nb_{0.1}O_{3- δ}, P_{Max} is 397 mW cm⁻² [48]; (Ba_{0.95}La_{0.05})FeO_{3- δ} is 401 mW cm⁻² [55]; and BaZr_{0.2}Fe_{0.6}Y_{0.2}O_{3- δ} is 322 mW cm⁻² [56].

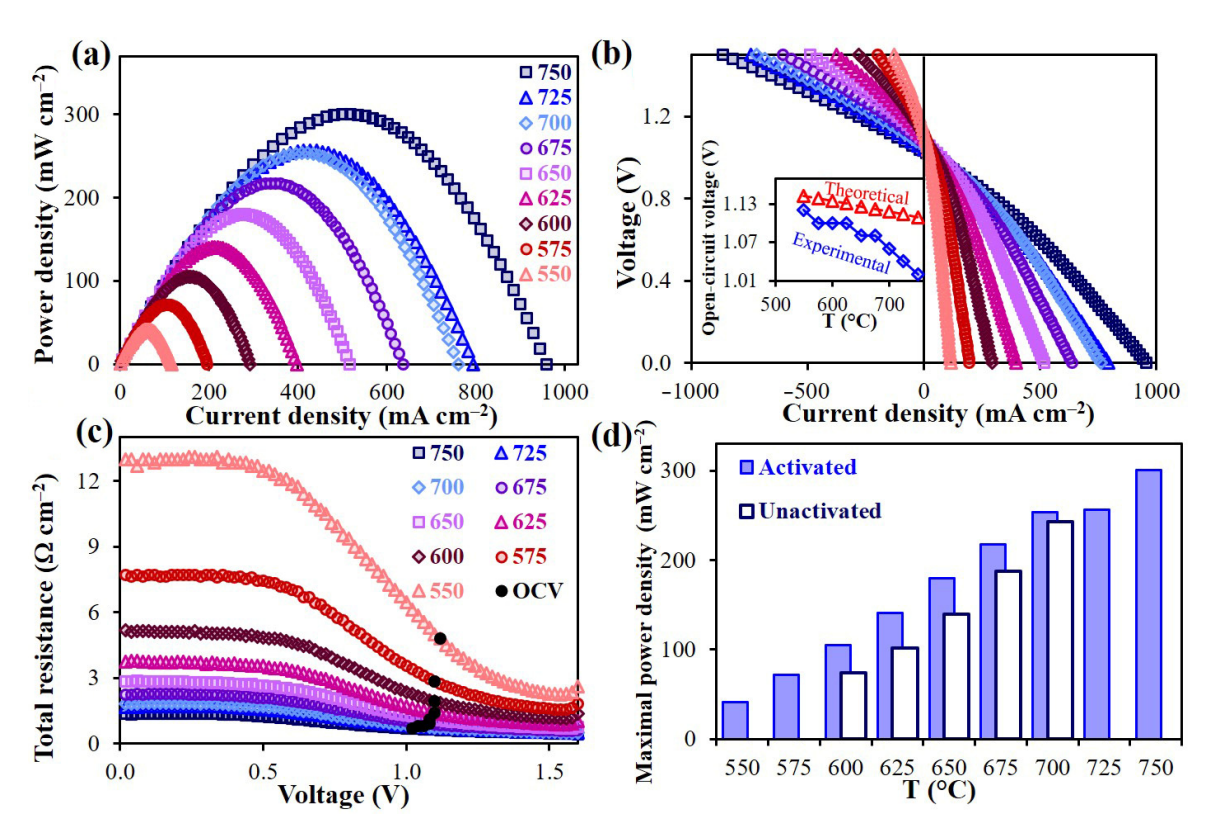


Figure 11. Power density dependencies of the electrochemical cell with BCZYF0.6 cathode (a), voltammetric characteristics (b), total resistances (c), and comparison of the maximum cell power densities before and after electroactivation (d).

The current-voltage characteristics of the reversible proton-conducting cell and the temperature dependencies of the open-circuit voltages (OCV) are shown in Figure 11b. At $550\,^{\circ}$ C, the OCV is $1.12\,$ V; this decreases with the increasing temperature to $1.02\,$ V at $750\,^{\circ}$ C. These values are slightly lower than the theoretical OCV values (inset in Figure 11b). In addition, as the temperature increases, the difference between the theoretical and experimental values of OCV becomes more noticeable. Since, as confirmed by SEM, the electrolyte membrane has a dense, impermeable microstructure, the difference in OCV values can be explained by the realization of electron-hole transport in the electrolyte [57,58].

Figure 11c shows the total PCFC resistances in DC measurements. When the cell operation mode is switched from fuel to electrolytic, there is a significant increase in the total resistance of the PCFC. Moreover, this increase is more significant when temperature decreases. This may be due to the features of the fuel and air electrodes during the change in the cell operation modes.

Previously, we published the research of PCFC with the air electrode of BaFe $_{0.6}$ Ce $_{0.1}$ Zr $_{0.2}$ Y $_{0.1}$ O $_{3-\delta}$ composition, which was not subjected to electrochemical activation [46]. Figure 11d shows a histogram comparing the maximum power densities for electrochemical cells with air electrode BCZYF0.6 before and after electroactivation. Despite the fact that the temperature range presented in the earlier work was smaller than this range, the tendency

Catalysts **2022**, 12, 1421 11 of 16

for improved power characteristics in cells with modified cathodes under operational conditions is evident.

2.3.3. Polarization Characteristics of the Air Electrode

The impedance spectra of electrochemical cells at 600 °C with activated and nonactivated air electrodes of BCZYF0.6 composition are shown in Figure 12a. Similar to the case of SDCs, activation insignificantly affects the course of the P_1 process. In turn, P_2 significantly decreases after the introduction of electrochemically active PrO_x nanoparticles. The ohmic (R_0) , polarization (R_p) , and total (R_{total}) resistances of the electrochemical cell were calculated based on the obtained spectra. Figure 12b,c compares the polarization and total resistances of electrochemical cells before and after activation of the air electrode. Here, it can be seen that the modification of the cathode with PrO_x nanoparticles has a favorable effect on the value of the polarization resistance of the cell, leading to its decrease and, as a consequence, to a decrease in the total resistance of the PCFC. The partial resistances of the electrochemical cell with the electrode composition BCZYF0.6 modified by PrO_x are shown in Figure 12d. At 550 °C, the polarization resistance contribution exceeds the ohmic resistance (3.35 Ω ° cm² vs. 1.35 Ω ° cm²). A further increase in temperature leads to a decrease in polarization resistance to $0.15 \,\Omega^{\circ} \text{cm}^2$ at 750 °C. In turn, the ohmic resistance determines the overall cell resistance at temperatures above 600 °C, indicating that the transport properties of the electrolyte limit the performance of the presented PCFC.

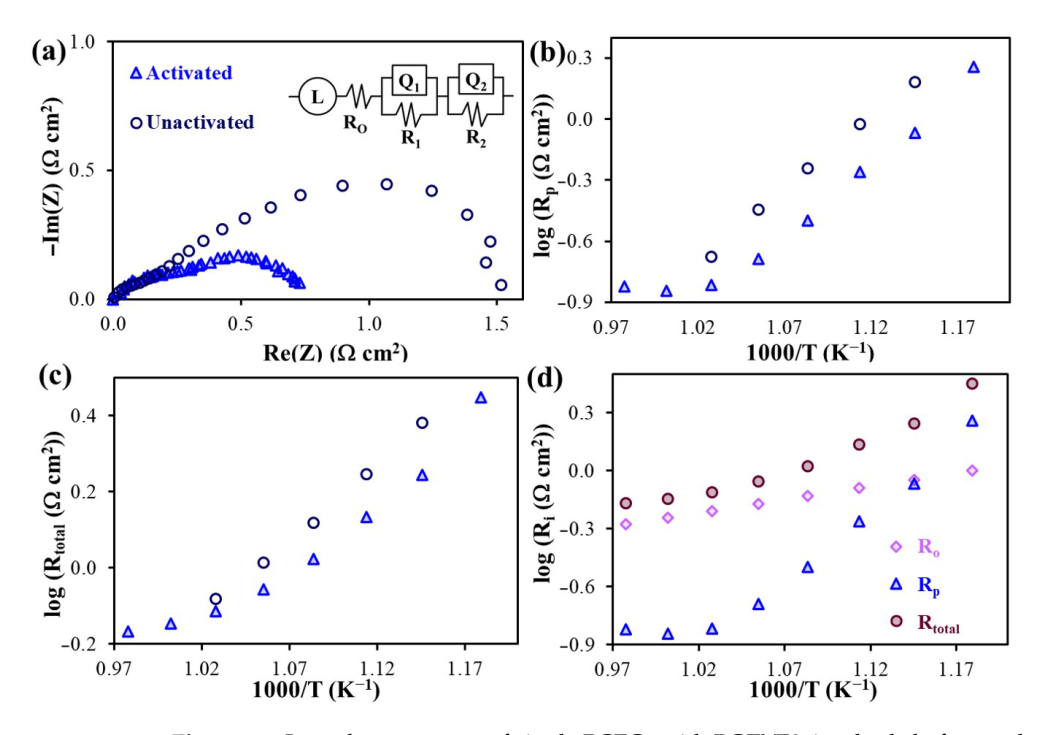


Figure 12. Impedance spectra of single PCFCs with BCZYF0.6 cathode before and after electroactivation (**a**), comparison of polarization (**b**) and total (**c**) resistances of single cells, partial resistances of electrochemical cell with cathode modified with PrO_X nanoparticles (**d**).

3. Materials and Methods

3.1. Preparation of Powders and Production of Ceramic Materials

Complex oxide powders based on BaFe_xCe_{0.7-x}Zr_{0.2}Y_{0.1}O_{3- δ} (BCZYFx, x = 0.5, 0.6, 0.7) and the electrolyte BaCe_{0.5}Zr_{0.3}Y_{0.1}Yb_{0.1}O_{3- δ} (BCZYYb) powder were prepared using a citrate-nitrate combustion (CNC) method [59]. Precursor materials were barium-, iron-, cerium-, and yttrium nitrates, as well as zirconium oxynitrate (from Alfa Aesar). Citric acid was used as a complexing agent and fuel according to the CNC method in a molar ratio of 1:1 between total metal cations and citric acid. The compounds were dissolved in a minimal amount of distilled water in a heat-resistant beaker. For the complete dissolution of

Catalysts **2022**, 12, 1421 12 of 16

the salts, the obtained mixture was heated to 100 °C and maintained at this temperature for 10 min. After obtaining a homogeneous solution, it was evaporated at 200 °C to form a gel-like mass. A subsequent increase in temperature up to 370 °C led to a spontaneous combustion followed by the formation of highly dispersed powders. After homogenization, using an agate mortar and pestle, the powders were subjected for a two-step synthesis with intermediate grinding at 1050 (5° h) and 1100 °C (5° h).

3.2. Fabrication of the Electrochemical Cells

To permit the further electrochemical studies of symmetrically designed cells (SDCs) with a composition of BCZYFx | BCZYYb | BCZYFx, the electrolyte powder was used to form dense electrolyte plates using a tape-calendaring method. Subsequently, the same electrolyte was used to obtain a half-cell with a configuration (NiO-BCZYYb)_{supp} | (NiO–BCZYYb)_{funct} | BCZYYb. For this purpose, individual films of the supporting (NiO:BCZYYb:starch = 60:40:20) and functional (NiO:BCZYYb = 55:45) anodes and electrolyte were preliminarily obtained. To prepare the films, the corresponding powders were ground in a mixture acetone and benzene, after which an organic binder (rubber and dibutyl phthalate) was added. The obtained suspensions were dried and thin films of 0.2 mm in thickness for the electrolyte and functional anode layers and 0.8 mm in thickness for the supporting anode layer were formed from the prepared plastic mass using a tape-calendaring method. Next, the prepared films were rolled together to produce a multilayer plate with a thickness of 0.8–0.9 mm. The multistage sintering of the multilayer plate comprised the following stages: Slow burn-out of the organic binder by heating to 900 °C (heating rate of 1 °C/min); heating to 1450 °C at a rate of 1.5 °C/min; isothermal holding at 1450 °C for 5 h; slow cooling to room temperature with a rate of 1.7 °C/min.

An air electrode with an area of $0.5~\rm cm^2$ for both SDCs and a single PCFC was formed using the spraying method. For this purpose, the BCZYFx powders were milled in a planetary mill at 550 rpm for $0.5~\rm h$. The milled powder was placed in an agate mortar, then ethyl alcohol and an organic binder (a mixture of α -terpineol and ethylcellulose) were added in a ratio of 1:1 between the dry powder mass and the binder mass. Sintering of the sprayed electrode layers was carried out at $1100~\rm ^{\circ}C$ for $1~\rm h$.

The air electrodes of SDCs were electroactivated by iteratively infiltrating them with an alcoholic solution of praseodymium nitrate. To control the level of their mass growth, all the samples were weighed beforehand. After applying a 50% alcohol salt solution to the porous cathodic layer for 2 min, the excess of alcohol solution on the cathode surface was removed with a dry paper towel, and the sample was air-dried. Following each impregnation, the mass change in the air-dried sample was measured. The infiltration of the porous electrode was performed until the sample mass had increased by 10%. Next, the infiltrated samples were calcined at $600\,^{\circ}\text{C}$ for 1 h to form nanoparticles of electrochemically active additives.

The air electrode of the PCFC with a structure of (NiO-BCZYb) $_{supp} + (NiO-BCZYb)_{funct} + BCZYb + BCZYF0.6_{porous}$ was activated by alcoholic solutions of praseodymium nitrate in the same manner.

3.3. Characterization of Materials

The phase composition of BCZYFx powder materials was identified using X-ray diffraction analysis (XRD, Rigaku MiniFlex 600, CuK α 1 emission) at room temperature in the $2\theta = 20^{\circ}-80^{\circ}$ angle range with a step of 0.02° .

Scanning electron microscopy (SEM, TESCAN VEGA, Tescan s.r.o.) was used both to analyze the thickness and density/porosity of the corresponding cell layers, as well as to study the distribution of electrochemically active particles of modifiers over the volume of the porous electrode.

3.4. Electrochemical Measurements

The polarization resistances of the studied electrodes before and after electroactivation on SDCs were measured by electrochemical impedance spectroscopy (EIS) using an Amel

Catalysts **2022**, 12, 1421 13 of 16

2550 potentiostat/galvanostat (Italy) in combination with a MaterialsM 520 frequency analyzer (Italy). The measurements were performed in air at 500–800 °C within a frequency range of 9×10^{-3} – 5×10^{5} Hz with an amplitude voltage of 50 mV.

The electrochemical characteristics of the PCFC (before and after activation) were characterized by the EIS method at temperatures ranging from 550 to 700 °C using wet (~3% $\rm{H_2O}$) hydrogen as a fuel and wet (~3% $\rm{H_2O}$) air as an oxidizer. Impedance spectra were obtained in the frequency range of 1 \times 10⁻²–1 \times 10⁴ Hz with an amplitude voltage of 50 mV. The obtained impedance spectra were analyzed using the method of equivalent circuits using the Zview software [60].

4. Conclusions

In this article, the investigated polarization characteristics of electrodes of BaFe $_x$ Ce $_{0.7-x}$ Zr $_{0.2}$ Y $_{0.1}$ O $_{3-\delta}$ composition are presented. In addition, the method of electrode activation by infiltration with praseodymium nitrate was successfully developed and applied. Studies of the whole concentration range of electrodes before and after electroactivation were carried out by EIS on symmetrical cells at 600–800 °C. Electroactivation at 750 °C was shown to reduce the polarization resistance by about 93, 50, and 27% for x = 0.5, 0.6, and 0.7, respectively. Considering the values of the initial level of polarization resistance and the degree of influence of infiltration on it, further studies on a single PCFC were carried out using a BCZYF0.6 cathode. It was found that the performance of the investigated cell as a whole is limited by the transport characteristics of the electrolyte material. Nevertheless, an increase in the power characteristics of a single PCFC with an activated BCZYF0.6 cathode as compared with a PCFC with a non-activated air electrode of the same composition, is noted. This allows for the described method of infiltration to be considered as a simple and affordable way to improve electrochemical characteristics.

Author Contributions: Conceptualization, L.R.T. and D.A.M.; methodology, G.K.V.; software, L.R.T. and G.N.S.; validation, L.R.T. and D.A.M.; formal analysis, A.V.K. and G.N.S.; investigation, L.R.T., A.V.K., G.N.S. and G.K.V.; data curation, D.A.M.; writing—original draft preparation, L.R.T. and D.A.M.; writing—review and editing, L.R.T. and D.A.M.; visualization, A.V.K., G.N.S. and L.R.T.; supervision, D.A.M.; project administration, L.R.T.; funding acquisition, L.R.T. All authors have read and agreed to the published version of the manuscript.

Funding: This work was financially supported by the President of the Russian Federation's scholarship to junior scientists and postgraduate students, no. CΠ-210.2022.1.

Data Availability Statement: Not applicable.

Acknowledgments: Scanning electron microscopy of symmetrical and fuel cells was performed at the Hydrogen Energy Laboratory of Ural Federal University. Other characterizations of powder and ceramic materials were carried out at the Shared Access Centre "Composition of Compounds" of Institute of High-Temperature Electrochemistry. We would also like to give a special thanks to Natalia Popova and Thomas Beavitt for the performed proofreading.

Conflicts of Interest: The authors declare no conflict of interest.

Catalysts **2022**, 12, 1421 14 of 16

Appendix A

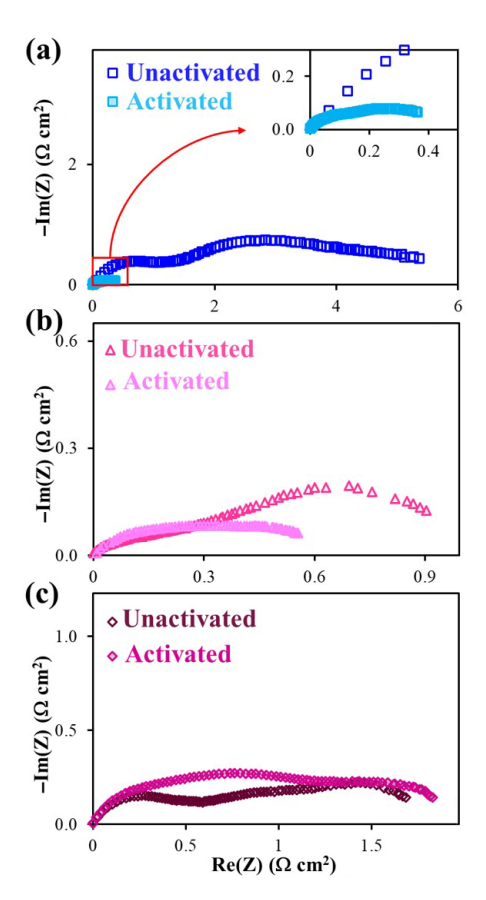


Figure A1. Nyquist coordinate impedance spectra at 600 °C obtained in SDC with BCZYF0.5 (a), BCZYF0.6 (b), and BZYF0.7 (c) electrodes before and after electroactivation.

References

- 1. Kupecki, J.; Niemczyk, A.; Jagielski, S.; Kluczowski, R.; Kosiorek, M.; Machaj, K. Boosting solid oxide electrolyzer performance by fine tuning the microstructure of electrodes—Preliminary study. *Int. J. Hydrogen Energy* **2022**. *In Press*. [CrossRef]
- 2. Ang, T.-Z.; Salem, M.; Kamarol, M.; Das, H.S.; Nazari, M.A.; Prabaharan, N. A comprehensive study of renewable energy sources: Classifications, challenges and suggestions. *Energy Strategy Rev.* **2022**, *43*, 100939. [CrossRef]
- 3. Guo, X.; Guo, Y.; Wang, J.; Zhang, H.; He, Z.; Wu, W.; Zhao, P. Energy, exergy and ecology performance prediction of a novel SOFC-AMTEC-TEG power system. *Appl. Therm. Eng.* **2022**, *217*, 119235. [CrossRef]
- 4. Tahir, N.N.M.; Baharuddin, N.A.; Samat, A.A.; Osman, N.; Somalu, M.R. A review on cathode materials for conventional and proton-conducting solid oxide fuel cells. *J. Alloys Compd.* **2022**, *894*, 162458. [CrossRef]
- 5. Dunyushkina, L.A. Solid oxide fuel cells with a thin film electrolyte: A review on manufacturing technologies and electrochemical characteristics. *Electrochem. Mater. Technol.* **2022**, *1*, 20221006. [CrossRef]
- 6. Yang, Y.; Zhang, Y.; Yan, M. A review on the preparation of thin-film YSZ electrolyte of SOFCs by magnetron sputtering technology. *Sep. Purif. Technol.* **2022**, *298*, 121627. [CrossRef]
- 7. Chasta, G.; Bhakar, U.; Suthar, D.; Himanshu; Lamba, R.; Dhaka, M.S. Impact of ethyl cellulose variation on microstructural and electrochemical properties of spin coated YSZ electrolyte thin films for SOFCs: Slurry composition evolution. *Ceram. Int.* **2022**, *in press*. [CrossRef]
- 8. Antonova, E.P.; Osinkin, D.A.; Bogdanovich, N.M. On a variation of the kinetics of hydrogen oxidation on Ni–BaCe(Y,Gd)O₃ anode for proton ceramic fuel cells. *Int. J. Hydrogen Energy* **2021**, *46*, 22638–22645. [CrossRef]
- 9. Akbar, M.; Qu, G.; Yang, W.; Gao, J.; Yousaf, M.; Mushtaq, N.; Wang, X.; Dong, W.; Wang, B.; Xia, C. Fast ionic conduction and rectification effect of NaCo_{0.5}Fe_{0.5}O₂-CeO₂ nanoscale heterostructure for LT-SOFC electrolyte application. *J. Alloys Compd.* **2022**, 924, 166565. [CrossRef]
- Nur Syafkeena, M.A.; Zainor, M.L.; Hassan, O.H.; Baharuddin, N.A.; Othman, M.H.D.; Tseng, C.-J.; Osman, N. Review on the preparation of electrolyte thin films based on cerate-zirconate oxides for electrochemical analysis of anode-supported proton ceramic fuel cells. J. Alloys Compd. 2022, 918, 165434. [CrossRef]

Catalysts **2022**, 12, 1421 15 of 16

11. Mojaver, P.; Chitsaz, A.; Sadeghi, M.; Khalilarya, S. Comprehensive comparison of SOFCs with proton-conducting electrolyte and oxygen ion-conducting electrolyte: Thermoeconomic analysis and multi-objective optimization. *Energy Convers. Manag.* 2020, 205, 112455. [CrossRef]

- Malik, V.; Srivastava, S.; Bhatnagar, M.K.; Vishnoi, M. Comparative study and analysis between Solid Oxide Fuel Cells (SOFC) and Proton Exchange Membrane (PEM) fuel cell—A review. Mater. Today Proc. 2021, 47, 2270–2275. [CrossRef]
- 13. Kasyanova, A.V.; Zvonareva, I.A.; Tarasova, N.A.; Bi, L.; Medvedev, D.A.; Shao, Z. Electrolyte materials for protonic ceramic electrochemical cells: Main limitations and potential solutions. *Mater. Rep. Energy* **2022**, 100158, *In Press.* [CrossRef]
- 14. Yi, Y.; Ran, R.; Wang, W.; Zhou, W.; Shao, Z. Perovskite-based nanocomposites as high-performance air electrodes for protonic ceramic cells. *Curr. Opin. Green Sustain. Chem.* **2022**, *38*, 100711. [CrossRef]
- 15. Rashid, N.L.R.M.; Samat, A.A.; Jais, A.A.; Somalu, M.R.; Muchtar, A.; Baharuddin, N.A.; Wan Isahak, W.N.R. Review on zirconate-cerate-based electrolytes for proton-conducting solid oxide fuel cell. *Ceram. Int.* **2019**, *45*, 6605–6615. [CrossRef]
- 16. Yoo, Y.; Lim, N. Performance and stability of proton conducting solid oxide fuel cells based on yttrium-doped barium cerate-zirconate thin-film electrolyte. *J. Power Sources* **2013**, 229, 48–57. [CrossRef]
- 17. Loureiro, F.J.A.; Nasani, N.; Reddy, G.S.; Munirathnam, N.R.; Fagg, D.P. A review on sintering technology of proton conducting BaCeO₃-BaZrO₃ perovskite oxide materials for Protonic Ceramic Fuel Cells. *J. Power Sources* **2019**, *438*, 226991. [CrossRef]
- 18. Guo, R.; Yang, L.; Wang, Y.; Xiao, Y.; Guan, R.; Wang, M.; He, T. Enhanced sintering and electrical properties of proton-conducting electrolytes through Cu doping in BaZr_{0.5}Ce_{0.3}Y_{0.2}O₃. *Ceram. Int.* **2022**, *48*, 11793–11804. [CrossRef]
- 19. Hossain, S.; Abdalla, A.M.; Jamain, S.N.B.; Zaini, J.H.; Azad, A.K. A review on proton conducting electrolytes for clean energy and intermediate temperature-solid oxide fuel cells. *Renew. Sustain. Energy Rev.* **2017**, *79*, 750–764. [CrossRef]
- 20. Zhang, W.; Hu, Y.H. Recent progress in design and fabrication of SOFC cathodes for efficient catalytic oxygen reduction. *Catal. Today* **2022**. *In Press*. [CrossRef]
- 21. da Silva, F.S.; de Souza, T.M. Novel materials for solid oxide fuel cell technologies: A literature review. *Int. J. Hydrogen Energy* **2017**, *42*, 26020–26036. [CrossRef]
- Pikalova, E.; Bogdanovich, N.; Kolchugin, A.; Ermakova, L.; Khrustov, A.; Farlenkov, A.; Bronin, D. Methods to increase electrochemical activity of lanthanum nickelate-ferrite electrodes for intermediate and low temperature SOFCs. *Int. J. Hydrogen Energy* 2021, 46, 35923–35937. [CrossRef]
- 23. Huang, Y.; Ding, J.; Xia, Y.; Miao, L.; Li, K.; Zhang, Q.; Liu, W. Ba $_{0.5}$ Sr $_{0.5}$ Co $_{0.8-x}$ Fe $_{0.2}$ Nb $_x$ O $_{3-\delta}$ ($x \le 0.1$) as cathode materials for intermediate temperature solid oxide fuel cells with an electron-blocking interlayer. *Ceram. Int.* **2020**, *46*, 10215–10223. [CrossRef]
- 24. Jhuang, J.-W.; Lee, K.-R.; Lee, S.-W.; Wang, B.; Xia, C.; Hung, I.M.; Tseng, C.-J. A triple ($e^-/O^{2-}/H^+$) conducting perovskite BaCo_{0.4}Fe_{0.4}Zr_{0.1}Y_{0.1}O_{3- δ} for low temperature solid oxide fuel cell. *Int. J. Hydrogen Energy* **2021**, *46*, 9767–9774. [CrossRef]
- 25. Pelosato, R.; Cordaro, G.; Stucchi, D.; Cristiani, C.; Dotelli, G. Cobalt based layered perovskites as cathode material for intermediate temperature Solid Oxide Fuel Cells: A brief review. *J. Power Sources* **2015**, 298, 46–67. [CrossRef]
- 26. Pikalova, E.; Bogdanovich, N.; Kolchugin, A.; Shubin, K.; Ermakova, L.; Eremeev, N.; Farlenkov, A.; Khrustov, A.; Filonova, E.; Sadykov, V. Development of composite LaNi_{0.6}Fe_{0.4}O_{3-δ}-based air electrodes for solid oxide fuel cells with a thin-film bilayer electrolyte. *Int. J. Hydrogen Energy* **2021**, *46*, 16947–16964. [CrossRef]
- 27. Yang, C.; Guo, R.; Jing, X.; Li, P.; Yuan, J.; Wu, Y. Degradation mechanism and modeling study on reversible solid oxide cell in dual-mode—A review. *Int. J. Hydrogen Energy* **2022**. *In Press*. [CrossRef]
- 28. Wei, Z.; Li, Z.; Wang, Z.; Zhao, Y.; Wang, J.; Chai, J. A free-cobalt barium ferrite cathode with improved resistance against CO₂ and water vapor for protonic ceramic fuel cells. *Int. J. Hydrogen Energy* **2022**, *47*, 13490–13501. [CrossRef]
- 29. Xia, Y.; Xu, X.; Teng, Y.; Lv, H.; Jin, Z.; Wang, D.; Peng, R.; Liu, W. A novel BaFe_{0.8}Zn_{0.1}Bi_{0.1}O_{3- δ} cathode for proton conducting solid oxide fuel cells. *Ceram. Int.* **2020**, *46*, 25453–25459. [CrossRef]
- 30. Subhashini, P.V.C.K.; Rajesh, K.V.D. Manufacturing method of BSCF cathode for low-temperature solid oxide fuel cell-A review. *Mater. Today Proc.* **2022**, *62*, 2357–2361. [CrossRef]
- 31. Su, R.; Lü, Z.; Jiang, S.P.; Shen, Y.; Su, W.; Chen, K. Ag decorated (Ba,Sr)(Co,Fe)O₃ cathodes for solid oxide fuel cells prepared by electroless silver deposition. *Int. J. Hydrogen Energy* **2013**, *38*, 2413–2420. [CrossRef]
- 32. Wang, Z.; Wang, Y.; Wang, J.; Song, Y.; Robson, M.J.; Seong, A.; Yang, M.; Zhang, Z.; Belotti, A.; Liu, J.; et al. Rational design of perovskite ferrites as high-performance proton-conducting fuel cell cathodes. *Nat. Catal.* **2022**, *5*, 777–787. [CrossRef]
- 33. Tarutina, L.R.; Lyagaeva, J.G.; Farlenkov, A.S.; Vylkov, A.I.; Vdovin, G.K.; Murashkina, A.A.; Demin, A.K.; Medvedev, D.A. Doped (Nd,Ba)FeO₃ oxides as potential electrodes for symmetrically designed protonic ceramic electrochemical cells. *J. Solid State Electrochem.* **2020**, 24, 1453–1462. [CrossRef]
- 34. Jing, J.; Lei, Z.; Zheng, Z.; Wang, H.; Yang, Z.; Peng, S. Tuning oxygen vacancy of the Ba_{0.95}La_{0.05}FeO_{3-δ} perovskite toward enhanced cathode activity for protonic ceramic fuel cells. *Int. J. Hydrogen Energy* **2022**, 47, 35449–35457. [CrossRef]
- 35. Wan, J.; Li, Z.; Zang, H.; Sun, Y.; Zhao, Y.; Wang, Z.; Zhu, Z.; Wei, Z.; Zheng, Q. Ba $Zr_{0.1}Fe_{0.9-x}Ni_xO_{3-\delta}$ cubic perovskite oxides for protonic ceramic fuel cell cathodes. *Int. J. Hydrogen Energy* **2022**, 47, 9395–9407. [CrossRef]
- Porotnikova, N.M.; Osinkin, D.A. Recent advances in heteroatom substitution $Sr_2Fe_{1.5}Mo_{0.5}O_{6-\delta}$ oxide as a more promising electrode material for symmetrical solid-state electrochemical devices: A review. *Electrochem. Mater. Technol.* **2022**, *1*, 20221003. [CrossRef]
- 37. Osinkin, D.A. Precursor of $Pr_2NiO_{4+\delta}$ as a highly effective catalyst for the simultaneous promotion of oxygen reduction and hydrogen oxidation reactions in solid oxide electrochemical devices. *Int. J. Hydrogen Energy* **2021**, *46*, 24546–24554. [CrossRef]

Catalysts 2022, 12, 1421 16 of 16

38. Onrubia-Calvo, J.A.; Pereda-Ayo, B.; Bermejo-López, A.; Caravaca, A.; Vernoux, P.; González-Velasco, J.R. Pd-doped or Pd impregnated 30% La_{0.7}Sr_{0.3}CoO₃/Al₂O₃ catalysts for NO_x storage and reduction. *Appl. Catal. B* **2019**, 259, 118052. [CrossRef]

- 39. Osinkin, D.A.; Beresnev, S.M.; Bogdanovich, N.M. Influence of Pr_6O_{11} on oxygen electroreduction kinetics and electrochemical performance of $Sr_2Fe_{1.5}Mo_{0.5}O_{6-\delta}$ based cathode. *J. Power Sources* **2018**, 392, 41–47. [CrossRef]
- 40. Wei, Z.; Wang, J.; Yu, X.; Li, Z.; Zhao, Y.; Chai, J. Study on Ce and Y co-doped BaFeO_{3-δ} cubic perovskite as free-cobalt cathode for proton-conducting solid oxide fuel cells. *Int. J. Hydrogen Energy* 2021, 46, 23868–23878. [CrossRef]
- 41. Shannon Radii. Available online: http://abulafia.mt.ic.ac.uk/shannon/ptable.php (accessed on 17 October 2022).
- 42. Lyagaeva, J.; Medvedev, D.; Filonova, E.; Demin, A.; Tsiakaras, P. Textured BaCe_{0.5}Zr_{0.3}Ln_{0.2}O_{3-δ} (Ln=Yb, Y, Gd, Sm, Nd and La) ceramics obtained by the aid of solid-state reactive sintering method. *Scr. Mater.* **2015**, *109*, 34–37. [CrossRef]
- 43. ImageJ Wiki. Available online: https://imagej.net/ (accessed on 17 October 2022).
- 44. Tarutina, L.R.; Vdovin, G.K.; Lyagaeva, J.G.; Medvedev, D.A. Ba $Ce_{0.7-x}Zr_{0.2}Y_{0.1}Fe_xO_{3-\delta}$ derived from proton-conducting electrolytes: A way of designing chemically compatible cathodes for solid oxide fuel cells. *J. Alloys Compd.* **2020**, *831*, 154895. [CrossRef]
- Cui, J.; Wang, J.; Zhang, X.; Li, G.; Wu, K.; Cheng, Y.; Zhou, J. Low thermal expansion material Bi_{0.5}Ba_{0.5}FeO_{3-δ} in application for proton-conducting ceramic fuel cells cathode. *Int. J. Hydrogen Energy* 2019, 44, 21127–21135. [CrossRef]
- 46. Liu, H.; Zhu, K.; Liu, Y.; Li, W.; Cai, L.; Zhu, X.; Cheng, M.; Yang, W. Structure and electrochemical properties of cobalt-free perovskite cathode materials for intermediate-temperature solid oxide fuel cells. *Electrochim. Acta* 2018, 279, 224–230. [CrossRef]
- 47. He, W.; Fan, J.; Zhang, H.; Chen, M.; Sun, Z.; Ni, M. Zr doped BaFeO_{3- δ} as a robust electrode for symmetrical solid oxide fuel cells. *Int. J. Hydrogen Energy* **2019**, 44, 32164–32169. [CrossRef]
- 48. Wang, S.; Xu, J.; Wu, M.; Song, Z.; Wang, L.; Zhang, L.; Yang, J.; Long, W.; Zhang, L. Cobalt–free perovskite cathode BaFe_{0.9}Nb_{0.1}O₃ for intermediate–temperature solid oxide fuel cell. *J. Alloys Compd.* **2021**, *872*, 159701. [CrossRef]
- 49. Zhou, X.; Hou, N.; Gan, T.; Fan, L.; Zhang, Y.; Li, J.; Gao, G.; Zhao, Y.; Li, Y. Enhanced oxygen reduction reaction activity of BaCe_{0.2}Fe_{0.8}O_{3-δ} cathode for proton-conducting solid oxide fuel cells via Pr-doping. *J. Power Sources* **2021**, 495, 229776. [CrossRef]
- 50. Gou, Y.; Li, G.; Ren, R.; Xu, C.; Qiao, J.; Sun, W.; Sun, K.; Wang, Z. Pr-Doping Motivating the Phase Transformation of the BaFeO_{3-δ} Perovskite as a High-Performance Solid Oxide Fuel Cell Cathode. *ACS Appl. Mater. Interfaces* **2021**. *In Press.* [CrossRef]
- Adler, S. Limitations of charge-transfer models for mixed-conducting oxygen electrodes. Solid State Ion. 2000, 135, 603

 –612. [CrossRef]
- 52. Tarutin, A.P.; Vdovin, G.K.; Medvedev, D.A.; Yaremchenko, A.A. Fluorine-containing oxygen electrodes of the nickelate family for proton-conducting electrochemical cells. *Electrochim. Acta* **2020**, 337, 135808. [CrossRef]
- 53. Tarutin, A.P.; Lyagaeva, J.G.; Medvedev, D.A.; Bi, L.; Yaremchenko, A.A. Recent advances in layered Ln₂ NiO_{4+δ} nickelates: Fundamentals and prospects of their applications in protonic ceramic fuel and electrolysis cells. *J. Mater. Chem. A* **2021**, *9*, 154–195. [CrossRef]
- 54. Wu, M.; Cai, H.; Jin, F.; Sun, N.; Xu, J.; Zhang, L.; Han, X.; Wang, S.; Su, X.; Long, W.; et al. Assessment of cobalt–free ferrite–based perovskite $Ln_{0.5}Sr_{0.5}Fe_{0.9}Mo_{0.1}O_{3-\delta}$ (Ln = lanthanide) as cathodes for IT-SOFCs. *J. Eur. Ceram. Soc.* **2021**, *41*, 2682–2690. [CrossRef]
- 55. Belotti, A.; Wang, Y.; Curcio, A.; Liu, J.; Quattrocchi, E.; Pepe, S.; Ciucci, F. The influence of A-site deficiency on the electrochemical properties of $(Ba_{0.95}La_{0.05})_{1-x}FeO_{3-\delta}$ as an intermediate temperature solid oxide fuel cell cathode. *Int. J. Hydrogen Energy* **2022**, 47, 1229–1240. [CrossRef]
- 56. Wu, Y.; Li, K.; Yang, Y.; Song, W.; Ma, Z.; Chen, H.; Ou, X.; Zhao, L.; Khan, M.; Ling, Y. Investigation of Fe-substituted in BaZr_{0.8}Y_{0.2}O_{3-δ} proton conducting oxides as cathode materials for protonic ceramics fuel cells. *J. Alloys Compd.* **2020**, *814*, 152220. [CrossRef]
- 57. Zvonareva, I.; Fu, X.-Z.; Medvedev, D.; Shao, Z. Electrochemistry and energy conversion features of protonic ceramic cells with mixed ionic-electronic electrolytes. *Energy Environ. Sci.* **2022**, *15*, 439–465. [CrossRef]
- 58. Huang, Y.; Qiu, R.; Lian, W.; Lei, L.; Liu, T.; Zhang, J.; Wang, Y.; Liu, J.; Huang, J.; Chen, F. Review: Measurement of partial electrical conductivities and transport numbers of mixed ionic-electronic conducting oxides. *J. Power Sources* **2022**, *528*, 231201. [CrossRef]
- 59. Babu, A.; Tirumalarao, D.; Das, S.; Dixit, V.; Sruthy, S.P.; Vijayan, V.; Jaiswal-Nagar, D. Effect of pH variation on citrate nitrate sol-gels obtained from auto-combustion method: Synthesis, calculations and characterisations of extremely dense BaZrO₃ ceramic. *Open Ceram.* **2022**, *12*, 100303. [CrossRef]
- 60. ZView®For Windows—Scribner Associates. Available online: http://www.scribner.com/software/68-general-electrochemistr3 76-zview-for-windows/ (accessed on 17 October 2022).